Unveiling the Influence of Absorber Thickness on Efficient Sb2(S, Se)3 Solar Cells Through Controlled Chemical Bath Deposition

Jun Zhao, Xuerui Li, Junhui Lin, Xiaofang Zhao, Muhammad Ishaq, Shuo Chen, Zhuanghao Zheng, Zhenghua Su, Xianghua Zhang, Guang-Xing Liang

Unveiling the Influence of Absorber Thickness on Efficient $Sb_2(S, Se)_3$ Solar Cells Through Controlled Chemical Bath Deposition

Jun Zhao[1#], Xuerui Li[1#], Junhui Lin[1,2],Xiaofang Zhao[2*], Muhammad Ishaq[1], Shuo Chen[1], Zhuanghao Zheng[1], Zhenghua Su[1], Xianghua Zhang[3], Guang-Xing Liang[1]*

[1.] *Shenzhen Key Laboratory of Advanced Thin Films and Applications, Key Laboratory of Optoelectronic Devices and Systems of Ministry of Education and Guangdong Province, College of Physics and Optoelectronic Engineering, Shenzhen University, Shenzhen 518060, Guangdong, P. R. China.*

[2.] *International School of Microelectronics, Dongguan University of Technology, Dongguan 523000, Guangdong, P. R. China*

[3.] *Institut des Sciences Chimiques de Rennes, UMR 6226, Rennes, F-35000, France*

[#] Jun Zhao and Xuerui Li contributed equally.

* Corresponding author. E-mail: 13669872773@163.com (Prof. Lin)

zhaoxf@dgut.edu.cn (Prof. Zhao)

Keywords: $Sb_2(S, Se)_3$; Photovoltaic device; Efficiency; Chemical bath deposition

Abstract

More focus has been placed in recent years on the most promising $Sb_2(S, Se)_3$. Because of its black-box character, the hydrothermal process has drawbacks, such as difficulties managing variables like pH, temperature, and chemical reactions. To overcome these challenges, a monitored and straightforward solution process was developed, enabling the wide-scale production of $Sb_2(S, Se)_3$ devices. This study carefully examined the impact of $Sb_2(S, Se)_3$ absorber thickness on the performance of photovoltaic devices. By effectively suppressing the recombination of chargest the $Sb_2(S, Se)_3$/CdS interface and reducing interfacial and bulk defects, a carefully managed optimum thickness improved the device's carrier transport mechanism. We found that solar cells with a light absorber thickness of approximately 210 nm had a smaller Urbach energy compared to solar cells with a thickness of approximately 95 nm, indicating a lower number of defect states. Additionally, the concentration of bulk and interface defects was lower in solar cells with a thickness of approximately 210 nm compared to those with a thickness of approximately 95 nm. Thus, a $Sb_2(S, Se)_3$ device with about 210 nm thick light absorber exhibited high efficiency of 5.51%, indicating a thickness-controlled CBD process with great potential to design a high-performance solar cell.

1. Introduction

There have been a growing variety of innovative semiconductor photovoltaic materials generated to support the quick and high-quality advancement of photovoltaic technology. Over the last decade, thin-film photovoltaic devices based on GaAs, CdTe, Cu (In,Ga)Se_2, and other photovoltaic materials have received more and more attention owing to their exceptional photovoltaic performances [1-3]. However, the rarity of Te, toxicity of As, and the expensive In and Ga are noteworthy difficulties that restrict their widespread deployment [4]. Thus, it is indispensable to find a suitable and optimal photovoltaic semiconductor materials. Among various photovoltaic materials, the non-toxic and earth-abundant $Sb_2(S,$

$Se)_3$ absorber has been recognized an potential photovoltaic semiconductor film because of its suitable absorption coefficient, ideal band gap, and outstanding stability [5-7]. Being a potential photoactive semiconductor material, developing a proper process for the $Sb_2(S, Se)_3$ fabrication having larger grain size, compact surface morphology, and best defect properties is an crucial factor in the development of devices' photovoltaic performance.

To this end, $Sb_2(S, Se)_3$ film employs a variety of preparation processes, including pulsed laser deposition (PLD), vapor transport deposition (VTD), rapid thermal evaporation (RTE), spin-coating, hydrothermal deposition (HD) and chemical bath deposition (CBD) [8-13]. In 2019, the RTE and VTD processes were used to fabricate the $Sb_2(S, Se)_3$ photovoltaic devices, but their power conversion efficiency (PCE) was lower than 7% [8]. In 2020, Chen et al. used pulsed laser deposition (PLD) to prepared $Sb_2(S, Se)_3$ photovoltaic devices reached a PCE of 7.05% [10]. Meanwhile, the solution processes develop the $Sb_2(S, Se)_3$ photovoltaic device. Chen's team achieved a PCE of $Sb_2(S, Se)_3$ device as high as 7.82% through a hydrothermal method in 2019 [14]. In 2021, the highest PCE of hydrothermal fabricated $Sb_2(S, Se)_3$ devices reach about 10.7% [15]. Practically it is evident that the solution process has certain advantages over the vacuum process. Despite achieving a PCE of over 10% in photovoltaic devices using the hydrothermal method, the $Sb_2(S, Se)_3$ growth mechanism through this method has remained elusive. This is primarily due to the challenges in real-time monitoring of crucial factors such as pH, temperature, and chemical reactions within the hydrothermal solution. In addition, it is challenging to fabricate large-area solar cells using this technique. Thus, a monitorable and simple solution method with the capability of large-scale fabrication is explored to synthesize $Sb_2(S, Se)_3$ devices.

CBD is an ideal process that offers many merits over hydrothermal process. For example, (i) the deposition of low-cost and low-temperature; (ii) real-time monitoring of precursors to unveil preparation method and growth of thin film; (iii) large-scale preparation of devices; (iv) continuous raw material replenishment, which boosts overall capacity and opens the door to

possible research into V-shape bandgap engineering [13]. The CBD method is more flexible than the hydrothermal method. It proves that this method can prepare the high-quality devices. Herein, for the fist time, we used a simple and monitor CBD process to deposit the $Sb_2(S, Se)_3$ devices. The reaction time was monitored during the entire reaction. The thickness of $Sb_2(S, Se)_3$ layers was optimized carefully and the influence mechanism of absorber thickness on solar cells was studied. Consequently, our champion $Sb_2(S,Se)_3$ device delivered an encouraging PCE of 5.5 %.

2. Experimental details

2.1. Preparation of CdS buffer layer

Firstly, distilled (DI) water, detergent, and ethanol were used to ultrasonically clean FTO glass, followed by a drying process of N_2 flow. A compact CBD based CdS layer was prepared on the surface of FTO glass substrates from a solution prepared with deionized water, thiourea (0.75 M), NH_3OH aqueous solution, and cadmium sulfate (0.015 M). Afterward, the glass substrates were dipped for at least 8 minutes 30 seconds while stirring constantly in the solution maintained at 85 ℃. Place the CdS layer in the oven to remove solution for 20 minutes. The corresponding CdS layers were then spin-coated with $CdCl_2$/methanol solution and annealed for 6 minutes each at 100 ℃ and 400 ℃, respectively.

2.2. Preparation of Sb_2Se_3 solar cells

The CBD method was further used to deposit a layer of $Sb_2(S, Se)_3$. The $C_4H_4KO_7Sb{\cdot}0.5H_2O$ (20 mM), $Na_2S_2O_3{\cdot}\ 5H_2O$ (80 mM), and selenourea (CH_4N_2Se) (4.5 mM) solution were used to make the CBD solution, which was then mixed into DI water with 40 mL and stirred to prepare a light yellow semitransparent solution. The FTO/CdS samples were immersed in light yellow semitransparent solution and were allowed to soak in a water bath maintained at 95℃ for 2 hours, 3 hours, 4 hours , and 5 hours, respectively. To obtain a well crystalline $Sb_2(S,Se)_3$, the as deposited layers were annealed in the glove box at 310℃. The as deposited

layers were put into the vacuum oven at 110 ℃ for 1 min. According the our previous work [16], to obtain a well crystalline $Sb_2(S,Se)_3$, the as deposited layers were annealed in the glove box at 350℃for 10 min. We used the heating platform to anneal. The thickness of $Sb_2(S,Se)_3$ absorber with reaction times (CBD processing time) of 2h, 3h, 4h and 5h were 95 nm, 128 nm, 210 nm, and 250 nm, respectively. Afterward, the hole transport layer (HTL) of spiro-OMeTAD (Advanced Election Technology Co., Ltd) was deposited via the spin coating on the FTO/CdS/$Sb_2(S,Se)_3$ surface. Lastly, the Au electrode was deposited using the thermal evaporation method to obtained a photovoltaic device architecture of FTO/CdS/$Sb_2(S,Se)_3$/Spiro-oMeTAD/Au. The as fabricated solar cells designed with different $Sb_2(S,Se)_3$ were designated as 2H, 3H, 4H, and 5H, respectively. The fabrication process of the device is depicted in Fig. 1. The prepared materials for each layer of solar cells are shown in Table S1.

2.3. Characterizations

The crystal phases of samples were measured by X-ray diffraction (XRD, Ultima-iv) using CuK_α radiation. We used the scanning electron microscope (SEM, Zeiss SUPRA 55) to analyze the morphologies of devices. Under standard conditions (100 mW/cm^2, AM 1.5 G), the current density-voltage of photovoltaic device was tested using the multi-meter (Keithley, 2400 Series). In addition, the multi-meter (Keithley, 2400 Series) was also used to characterize the dark current density-voltage of samples. We used the Keithley 2400 source meter with the Zolix SCS101 system to characterize the external quantum efficiency (EQE) of devices. A 355 nm pulsed laser light source was utilized to excite the sample, and the voltage signals were recorded byan oscilloscope (Tektronix TDS 3054C, 500 MHz) to perform transient surface photovoltage (TSPV). To perform capacitance-voltage (*C-V*) and drive level capacitance (*DLCP*) characterization, Keithley 4200A-SCS and JANIS cryogenic platform was utilized. To study the recombination mechanism, CHI600E electrochemical workstation was utilized to conduct electrochemical impedance spectroscopy (EIS). For deep-level

transient spectroscopy (DLTS), HERA (FT-1030) system fitted with a VPF-800 Janis cryostat controller was used.

3. Result and discussion

To investigate the influence absorber layer thickness on device performance, we fabricated $Sb_2(S, Se)_3$ film with different reaction times (2h, 3h, 4h, and 5h). These films were then incorporated into the device structure, as revealed in Figure 1(e). The J-V responses of the photovoltaic devices, labeled as 2H, 3H, 4H, and 5H, displayed distinct characteristics that reflected the role of absorber thickness. Notably, the PCE of the device exhibited a gradual increase from 3.52% to 5.51% as the reaction time (and therefore thickness) increased up to 4H. However, upon further increasing the absorber thickness, the efficiency decreased to 4.7%. This observation suggests that there is an optimal absorber thickness for achieving the highest PCE in $Sb_2(S, Se)_3$ photovoltaic devices. The photovoltaic parameters of 2H, 3H, 4H and 5H photovoltaic devices are listed in Table 1. For comparative analysis, we elected 2H and 4H devices to further investigate the role of absorber thickness in the device performance, as they exhibited an evident difference in their performance parameters. Fig. 2(a) illustrates the *J-V* of photovoltaic devices. The 2H based solar could deliver a J_{SC} of 10.99 mA/cm^2, V_{OC} of 0.540 V, and PCE of 3.52%. While 4H device exhibited 5.51% PCE, with a Fill factor of 51.93%, a V_{OC} of 0.647 V, and a J_{SC} of 17.23 mA/cm^2. We found that the series resistance R_S of 4H solar cells is higher than that of 2H solar cells. In addition, the shunt resistance R_{sh} of 4H solar cells is smaller than that of 2H solar cells. According to the reported literature [17], the FF of 4H solar cells should be lower than that of 2H solar cells. A decline in the device performance for further prolonged reaction time-based devices can be ascribed to the excessive inclusion of Se in the film, which tends to reduce the band gap of the film. The EDS analysis of all samples (Table 2) can prove this argument. As the reaction times of CBD increase from 2h to 5h, excessive inclusion of Se in the film can be observed in EDS results.

This also can be a possible explanation for the drop in V_{OC} (open-circuit voltage) [18]. The increased thickness of the film, which makes it necessary for the excitons to travel a greater distance within it, is another element that contributes to poor charge extraction and a decline in the fill factor (FF) [19]. The photovoltaic parameters of 2H, 3H, 4H and 5H solar cells were listed in Table 2. The EQE spectra of 2H and 4H solar cells are plotted in Fig. 2(b). The 4H device presented high EQE for the whole absorption spectrum of $Sb_2(S,Se)_3$. The EQE values were more than 40% and peak value reached over 80% for 350–800 nm wavelength range. The integrated short-circuit current densities derived from the EQE results was 15.12 mA/cm^2, which is close to the J_{SC} of 4H device derived from the *J-V* curve. On the other hand, the peak value of EQE spectrum for 2H device could hardly reach 50%, with an integrated J_{SC} of 9.35 mA/cm^2. The EQE data can be utilized to determine the $Sb_2(S,Se)_3$ layer's EQE-dependent bang gap with reaction times of 2h and 4h (Fig. 2(c)). For 2H and 4H solar cells, respectively, a band gap of 1.77 eV and 1.65 eV was extracted from the EQE-dependent band gap of absorber layer, which is close to the reported value in the paper [20]. An essential measure utilized to define the band tail states caused by disorders, defects, and impurities in $Sb_2(S, Se)_3$ layers is the Urbach energy (E_U) of solar cells [21]. According to Fig. 2(d), the Urbach energies of 2H and 4H solar cells obtained here are 40 meV and 34 meV, respectively. A lower E_U for 4H solar cells signifies that the absorber layer's proper reaction time resulted in the development of the proper stoichiometry and fewer defect states in the material. According to the reported literature, lower E_U for 4H solar cells means that the absorber layer of 4H solar cells has the larger absorption coefficient [22]. It indicates that the absorber layer of 4H solar cells is easier than that of 2H solar cells to create the photogenerated carriers, producing larger photocurrent. In addition, the lower E_U of absorber layer in 4H solar cells may have the superior conductivity than that of 2H solar cells. Another reported literature proves this argument [23]. Understanding the effect of the absorber layer's reaction times in devices requires in-depth examination. XRD was utilized to test the $Sb_2(S, Se)_3$ devices'

structural characteristics. Fig. 3(a) illustrates that the remaining diffraction peaks align with the reported peaks of $Sb_2(S, Se)_3$ films [24-26], with the exception of the peaks corresponding to FTO (marked as ♠) and CdS (marked as ♣). $Sb_2(S, Se)_3$ film has a higher peak intensity with a 4h reaction time than it does with a 2h reaction time. It indicates that the suitable reaction time promotes the $Sb_2(S, Se)_3$ absorber growth. Revealing the preferred tilted orientations for solar cells performance, particularly (221) emerged more evidently, while the tilted orientations (120) appeared to be slightly suppressed with increasing thickness of the absorber layer [27]. Scanning electron microscopic images of the surface morphologies of $Sb_2(S, Se)_3$ absorber layer with reaction times of 2h and 4h are portrayed in Fig. 3(b) and (c). The illustration shows that the $Sb_2(S, Se)_3$ surface has white particles (perhaps indicative of additional crystal phases), small grains and compact morphologies after a reaction time of 2h. While the 4h reaction time-based film exhibited the formation of large grains and a compact $Sb_2(S, Se)_3$ absorber. The surface morphologies of $Sb_2(S, Se)_3$ films are not adversely affected by the appropriate reaction time. In comparison to $Sb_2(S, Se)_3$ absorber layer with a reaction time of 2h, the grain sizes of $Sb_2(S, Se)_3$ absorber layer with reaction time of 4h are larger and more compact. The average grain size appeared to be 1.3 microns for 4h film, as estimated by the statistical distribution of grain size (Fig. 3(d)). The grain sizes of $Sb_2(S,Se)_3$ absorber with reaction times of 2h and 4h can be observed from Fig. 3(b) and (c). However, the thickness of absorber layer is too thin in Fig. 3(e) and (f), which is difficult to distinguish the detail cross-sectional morphology of $Sb_2(S,Se)_3$ absorber. Thus, The grain size from 1.2 to 1.5 um are difficult to find in Fig. 3 (f). The thickness of Au electrode, spiro-OMeTAD HTL, CdS and $Sb_2(S, Se)_3$ absorber layer are observed from cross-sectional images in Fig. 3(e) and (f). The absorber thickness of the 4H device is 210 nm, compared to 95 nm for the 2H device. The thickness of $Sb_2(S, Se)_3$ absorber apparently has a considerable impact on the photovoltaic performances of devices, as it may result in faster charge recombination chances and low light absorption capabilities if it is too thin.

Capacitance–voltage (C–V) and drive level capacitance profiling (DLCP) tests were performed to enumerate the defects in both types of solar cells prepared with different absorber thicknesses, (Fig. 4(a)). C–V analysis is an crucial technique to approximate the depletion width, the defect density, the built-in electric field, and the distribution of defect, which is sensitive to free carriers, bulk defects and interfacial defects [28,29]. Thus, the defects of $Sb_2(S,Se)_3$/CdS interface in devices were determined by the $N_{C\text{-}V}$-N_{DLCP} at 0 V . From equation 1, the $N_{C\text{-}V}$ and N_{DLCP} plots for 2H and 4H solar cells can be obtained [30-33].

$$\begin{cases} N_{C\text{-}V} = \dfrac{-2\varepsilon_{r,n}N_D}{\left(\dfrac{d(1/C^2)}{dV}\right)qA^2\varepsilon_0\varepsilon_{r,n}\varepsilon_{r,p}N_D + 2\varepsilon_{r,p}} \\ N_{DLCP} = -\dfrac{C_0^{\,3}}{2q\varepsilon_0\varepsilon_{r,p}A^2C_1} \\ x = \varepsilon_0\varepsilon_{r,p}A/C_0 \end{cases} \quad (1)$$

where, N_D stands for the carrier concentration of CdS buffer layer, A for the solar cell's effective area, C_0 and C_1 for two quadratic fitting parameters obtained from the *C-V* data, and ε_0 for the permittivity of free space. $\varepsilon_{r,n}$ and $\varepsilon_{r,p}$ depict the relative permittivity of CdS buffer layer and $Sb_2(S,Se)_3$ absorber layer. The calculated $N_{C\text{-}V}$ concentration for 2H and 4H device were 5.95×10^{15} cm^{-3} and 2.76×10^{15} cm^{-3}, while the N_{DLCP} concentration were 4.47×10^{15} cm^{-3} and 2.02×10^{15} cm^{-3}, respectively. For 2H and 4H solar cells, the measured interfacial defect concentrations are 1.48×10^{15} cm^{-3} and 7.4×10^{14} cm^{-3}, respectively. The lower interfacial defect concentration and interface recombination for 4H solar cell is indicated by the lower difference between the *DLCP* and the *C-V* values. These results demonstrate superior heterojunction properties for $Sb_2(S, Se)_3$/CdS benefited from an appropriate absorber layer thickness; thus surprising the most common defect-assisted Shockley–Read–Hall (SRH) recombination performances in the CBD-deposited $Sb_2(S,Se)_3$ photovoltaic devices [34,35]. Furthermore, 4H solar cell had a wider depletion width (W_d)

than 2H solar cell, demonstrating comparatively better carrier collection. Capacitance-voltage (*C-V*) of solar cells has been characterized in order to learn more about the depletion zone that is responsible for improved photovoltaic properties. Fig. 4(b) shows the $1/C^2$-V curves of 2H and 4H solar cells. The built-in voltage (V_{bi}) of 2H and 4H solar cells are 645 mV and 764 mV, respectively. The reason for the stark contrast between the two devices is the high built-in electric field and enhanced interface quality, which raise the V_{OC}, J_{SC} , and efficiency of 4H solar cell. Additionally, the minority carrier life time obtained from the TSPV analysis for 2H and 4H solar cells are 4.03 μS and 7.15 μS, signifying a reduced recombination upon the appropriate selection of absorber layer. As the reaction times of CBD increases to 5h, the $N_{C\text{-}V}$, N_{DLCP}, interfacial defect concentration, V_{bi}, W_d, and τ of 5H device are worse than that of 4H devices. Table 3 shows the $N_{C\text{-}V}$, N_{DLCP}, interfacial defect concentration, V_{bi}, W_d, and τ of all devices. The EIS analysis further authenticated a superior heterojunction quality for 4H device, as the EIS curved revealed the recombination resistances of 15000 Ω and 62000 Ω for 2H and 4H solar cells, respectively. This designates a constrained carrier recombination at the interface between $Sb_2(S, Se)_3$ and CdS by an appropriate absorber thickness.

To further authenticate the boosted properties of the 4H photovoltaic device, the PN-junction quality of 2H and 4H solar cells was systematically investigated. The dark *J-V* of photovoltaic devices are depicted in Fig. 5(a). Diode ideality factor (*A*), series resistance (*R*), Shunt conductance (*G*) and reverse-saturation current density (J_0) were calculated by equation 2 [18].

$$J = J_0 \exp\left[\frac{q}{AkT}(V - RJ)\right] + GV - J_L \tag{2}$$

Fig. 5(b) shows the dJ/dV vs V plot. The G of 2H and 4H solar cells are 2.80 mS/cm^2 and 0.49 mS/cm^2. The R and A values of the solar cells were calculated from dV/dJ against $(J+J_{SC})^{-1}$ in Fig. 5(c). The R of 2H and 4H solar cells are 4.97 Ω·cm^2 and 3.24 Ω·cm^2, respectively. In addition, the A of 2H and 4H solar cells are 2.24 and 1.93, respectively, indicating that the 4H

solar cell experiences less interface recombination. Basically, A refects the defect-assisted Shockley–Read–Hall (SRH) recombination in a solar cell. A lower A value (1<A<2) can rightly be ascribed to a better junction quality, and amended interfacial recombinations [19]. The J_0 for 2H and 4H solar cells, respectively, are 4.60×10^{-4} mA/cm^2 and 3.82×10^{-4} mA/cm^2, as shown in Fig. 5(d). All parameters proves that the appropriate absorber thickness controls the $Sb_2(S, Se)_3$/CdS interface recombination. To understand the impacts of absorber thickness on the bulk defect of absorber, the defect dynamics of the 2H and 4H solar cells is measure using the DLTS. The hole and electron traps, respectively, are represented by the positive and negative peaks [33]. The bulk defects types of 2H and 4H solar cells can be observed in Fig. 6(a). Only one hole trap is present in the 2H and 4H solar cells. Fig. 6(b) shows the activation energy E_A (E_T-E_V or E_C-E_T, where E_T, E_C, and E_V represent the defect energy level, conduction, and valence band level, respectively), where the H1 hole traps in both 2H and 4H solar cells are Sb vacancies (V_{Sb}) [36,37]. With reaction times of 2h and 4h, the defect concentrations (N_T) of the absorber layer are 5.10×10^{11} cm^{-3} and 4.47×10^{11} cm^{-3}, respectively. In contrast, the 4H solar cell has lower V_{Sb} defect concentrations than the 2H solar cell. It proves that the right absorber thickness can control charge recombination and lower the defect density of the Sb_2Se_3 absorber layer. Figure 6(c) displays the band edge positions and defect levels of 2H and 4H solar cells. In the 2H solar cell, H1 hole defects are observed at approximately 0.16 eV on the energy scale of the valence band (E_V). Conversely, in the 4H solar cell, H1 hole defects are found at around 0.386 eV on the E_V. The capture cross-section (σ) for the 2H and 4H solar cells are determined to be 9.51×10^{-16} cm^2 and 9.51×10^{-18} cm^2, respectively. Furthermore, the V_{Sb} defect in the 2H solar cell exhibits a $N_T \times \sigma$ value of 4.85×10^{-4} cm^{-1}, which is higher than the $N_T \times \sigma$ value of 4.87×10^{-7} cm^{-1} in the 4H solar cell. These results suggest that the 4H solar cells experience relatively lower charge recombination compared to the 2H solar cells [21]. The defect parameters of 5H device are worst than that of 4H device when the absorber thickness further increases. The Defects parameters of all Sb_2(S,

$Se)_3$ photovoltaic devices are summarized in Table 4. Thus, a meticulous optimization of the $Sb_2(S, Se)_3$ thickness results in improved surface morphology, reduction of bulk and interfacial defects, as well as advanced charge recombination resistance. This optimization also leads to the reduction of the reverse saturation current and ideality factor, ultimately resulting in an overall performance boost for the solar cell.

4. Conclusion

In conclusion, our comprehensive exploration using chemical bath deposition (CBD) has shed light on the influence of absorber thickness on the photovoltaic characteristics of $Sb_2(S, Se)_3$ devices. The crystal orientation, film morphology, bulk and interfacial defects, and charge transfer mechanism based on absorber layer thickness using this method were further investigated. An appropriate absorber thickness (210 nm) in solar cells exhibits a better carrier collection, less interface recombination at $Sb_2(S, Se)_3$/CdS, and prolonged minority carrier lifetime. In addition, the optimal absorber thickness reduces the bulk defect densities of absorber layer. A superstrate configured device (FTO/CdS/$Sb_2(S,Se)_3$/spiro-OMeTAD/Au) with a 210 nm thick absorber could deliver 5.51% efficiency (V_{OC} of 0.647 V, J_{SC} of 17.23 mA cm^2 and FF of 51.93%). A series of characterizations and data analysis of our high-efficiency device revealed that a thickness-controlled CBD process has great potential to design a high-performance photovoltaic device.

CRediT author statement

J Lin, X Zhao, X Zhang and G Liang conceptualized this study. J Zhao, X Li, J Lin and X Zhao conducted the experiment. J Lin, J Zhao, X Li and X Zhao performed the data analysis and write the manuscript. M Ishaq, S Chen, Z Zheng and Z Su helped to characterize and data analyze. All the authors revised the manuscript.

Acknowledgements

This work was supported by National Natural Science Foundation of China (No. 62074102),

Guangdong Basic and Applied Basic Research Foundation (2022A1515010979) China, Science and Technology plan project of Shenzhen (20220808165025003) China.

Data Availability Statement

Data available on request from the authors

References

[1] R. Cariou, J. Benick, F. Feldmann, O. Hohn, H. Hauser, P. Beutel, N. Razek, M. Wimplinger, B. Blasi, D. Lackner, M. Hermle, G. Siefer, S.W. Glunz, A.W. Bett, F. Dimroth, III-V-on-silicon solar cells reaching 33% photoconversion efficiency in two-terminal configuration, Nat. Energy 3 (2018) 326-333.

[2] J.M. Burst, J.N. Duenow, D.S. Albin, E. Colegrove, M.O. Reese, J.A. Aguiar, C.S. Jiang, M.K. Patel, M.M. Al-Jassim, D. Kuciauskas, CdTe solar cells with open-circuit voltage breaking the 1V barrier, Nat. Energy 1 (2016) 16015.

[3] A. Chirila, P. Reinhard, F. Pianezzi, P. Bloesch, A.R. Uhl, C. Fella, L. Kranz, D. Keller, C. Gretener, H. Hagendorfer, D. Jaeger, R. Erni, S. Nishiwaki, S. Buecheler, A.N. Tiwari, Potassium-induced surface modification of Cu(In, Ga)Se_2 thin films for high-efficiency solar cells, Nat. Mater. 12 (2013) 1107-1111.

[4] Y.Q. Zhao, S.Y. Wang, C. Li, B. Che, X.L. Chen, H.Y. Chen, R.F. Tang, X.M. Wang, G.L. Chen, T. Wang, J.B. Gong, T. Chen, X.D. Xiao, J.M. Li, Regulating deposition kinetics via a novel additive-assisted chemical bath deposition technology enables fabrication of 10.57 %-efficiency Sb_2Se_3 solar cells, Energy Environ. Sci. 15 (2022) 5118-5128.

[5] H. Lei, J. Chen, Z. Tan, G. Fang, Review of recent progress in antimony chalcogenide-based solar cells: materials and devices, Sol. RRL 3 (2019) 1900026.

[6] X. Wang, R. Tang, C. Wu, C. Zhu, T. Chen, Development of antimony sulfide-selenide $Sb_2(S,Se)_3$-based solar cells, J. Energy Chem. 27 (2018) 713-721.

[7] C. Jiang, J. Zhou, R. Tang, W. Lian, X. Wang, X. Lei, H. Zeng, C. Zhu, W. Tang, T. Chen,

9.7%-efficient $Sb_2(S,Se)_3$ solar cells with a dithieno[3,2-b:2',3'-d] pyrrolecored hole transporting material, Energy Environ. Sci. 14 (2021) 359-364.

[8] B. Yang, S.K. Qin, D.J. Xue, C. Chen, Y.S. He, D.M. Niu, H. Huang, J. Tang, In situ sulfurization to generate $Sb_2(Se1\text{-}xSx)_3$ alloyed films and their application for photovoltaics, Prog. Photovoltaics 25 (2017) 113-122.

[9] Y.L. Pan, X.B. Hu, Y.X. Guo, X.Y. Pan, F. Zhao, G.E. Weng, J.H. Tao, C.H. Zhao, J.C. Jiang, S.Q. Chen, P.X. Yang, J.H. Chu, Vapor transport deposition of highly efficient $Sb_2(S,Se)_3$ solar cells via controllable orientation growth, Adv. Funct. Mater. 31 (2021) 2101476.

[10] C. Chen, Y.W. Yin, W.T. Lian, L.F. Jiang, R.F. Tang, C.H. Jiang, C.Y. Wu, D. Gao, X.M. Wang, F. Fang, C.F. Zhu, T. Chen, Pulsed laser deposition of antimony selenosulfide thin film for the efficient solar cells, Appl. Phys. Lett. 116 (2020) 133901.

[11] C.Y. Wu, W.T. Lian, L.J. Zhang, H.H. Ding, C.H. Jiang, Y.Y. Ma, W.H. Han, Y.M. Li, J.F. Zhu, T. Chen, C.F. Zhu, Water additive enhanced solution processing of alloy $Sb_2(S_{1-x}Se_x)_3$ -based solar cells, Sol. RRL 4 (2020) 1900582.

[12] X.M. Wang, R.F. Tang, C.H. Jiang, W.T. Lian, H.X. Ju, G.S. Jiang, Z.Q. Li, C.F. Zhu, T. Chen, Manipulating the electrical properties of $Sb_2(S,Se)_3$ film for high-efficiency solar cell, Adv. Energy Mater. 10 (2020) 2002341.

[13] S. Li, S.C. Lu, Y. Lu, J.Y. Xue, K.H. Li, C. Chen, J. Tang, Efficient $Sb_2(S,Se)_3$ solar cells via monitorable chemical bath deposition, J. Mater. Chem. A 10 (2022) 11625-11635.

[14] C.H. Jiang, J.S. Yao, P. Huang, R.F. Tang, X.M. Wang, X.Y. Lei, H.L. Zeng, S. Chang, H.Z. Zhong, H.B. Yao, C.F. Zhu, T. Chen, Perovskite quantum dots exhibiting strong hole extraction capability for efficient inorganic thin film, Cell Rep. Phys. Sci. 1 (2020) 100001.

[15] Y.Q. Zhao, S.Y. Wang, C.H. Jiang, C. Li, P. Xiao, R.F. Tang, J.B. Gong, G.L. Chen, T. Chen, J.M. Li, X.D. Xiao, Regulating energy band alignment via alkaline metal fluoride

assisted solution post-treatment enabling $Sb_2(S,Se)_3$ solar cells with 10.7% efficiency, Adv. Energy Mater. 12 (2021) 2103015.

[16] M. Azam, Y.D. Luo, R. Tang, S. Chen, Z.H. Zheng, Z.H. Su, A. Hassan, P. Fan, H.L. Ma, T. Chen, G.X. Liang, X.H. Zhang, Organic chloride salt interfacial modified crystallization for efficient antimony selenosulfide solar cells, ACS Appl. Mater. Interfaces 14 (2022) 4276-4284.

[17] M, Yamaguchi, H. Tampo, H. Shibata, K.H. Lee, K. Araki, N. Kojima, Y. Ohshita, Analysis for non-radiative recombination and resistance loss in chalcopyrite and kesterite solar cells, Jpn. J. Appl. Phys. 60 (2021) SBBF05.

[18] M. Ishaq, H. Deng, S.J. Yuan, H. Zhang, J. Khan, U. Farooq, H.S. Song, J. Tang, Efficient double buffer layer $Sb_2(Se_xS_{1-x})_3$ thin film solar cell via single source evaporation, Sol. RRL 2 (2018) 1800144.

[19] C. Chen, Y. Zhao, S.C. Lu, K.H. Li, Y. Li, B. Yang, W.H. Chen, L. Wang, D.B. Li, H. Deng, F. Yi, J. Tang, Accelerated optimization of TiO_2/Sb_2Se_3 thin film solar cells by high-throughput combinatorial approach, 7 (2017) 1700866.

[20] Y. Lu, K.H. Li, X.K. Yang, S.C. Lu, S. Li, J.J. Zheng, L.C. Fu, C. Chen, J. Tang, HTL-free $Sb_2(S, Se)_3$ solar cells with an optimal detailed balance band gap, ACS Appl. Mater. Interfaces 13 (2021) 46858-46865.

[21] J.H. Lin, A. Mahmood, G.J. Chen, N. Ahmad, M.D. Chen, P. Fang, S. Chen, R. Tang, G.X. Liang, Crystallographic orientation control and defect passivation for high-efficient antimony selenide thin-film solar cells, Mater. Today Phys. 27 (2022) 100772.

[22] A.H. Ammar, A.A.M. Farag, M.S. Abo-Ghazala, Influence of Sb addition on the structural and optical characteristics of thermally vacuum evaporated Sb_XSe_{1-X} thin films, J. Alloy. Compd. 694 (2017) 752-760.

[23] W.W. Lin, N.W. Wang, Z.Y. Lan, Z. Fu, Z.P. Huang, L.M. Lin, Q.Y. Ye, S.Y. Chen, G.L. Chen, Construction of CdS/Sb_2Se_3 planar heterojunction by full vapor transport

deposition, Vacuum 206 (2022) 111544.

[24] X.Y. Pan, Y.L. Pan, L.J. Wang, C.H. Zhao, X.B. Hu, J.C. Jiang, B.C. Yang, S.Q. Chen, P.X. Yang, J.H. Chu, J.H. Tao, Interfacial engineering by applying double CdS structure electron transport layer for high-performance $Sb_2(S,Se)_3$ solar cells, Ceram. Int. 49 (2023) 22471-22478.

[25] X.Q. Shi, F. Zhang, S.Y. Dai, P.J. Zeng, J.L. Qu, J. Song, Nanorod-textured $Sb_2(S,Se)_3$ bilayer with enhanced light harvesting and accelerated charge extraction for high-efficiency $Sb_2(S,Se)_3$ solar cells, Chem. Eng. J. 437 (2022) 135341

[26] Y.L. Xing, H.F. Guo, J.J. Liu, S. Zhang, J.H. Qiu, N.Y. Yuan, J.N. Ding, high-efficiency $Sb_2(S,Se)_3$ solar cells with MoO_3 as a hole-transport layer, J. Alloy. Compd. 927 (2022) 166842.

[27] M. Ishaq, H. Deng, U. Farooq, H. Zhang, X.K. Yang, U.A. Shah, H.S. Efficient copper-doped antimony sulfide thin-film solar cells via coevaporation method, Sol. RRL 3 (2019) 1900305.

[28] X. Wen, C. Chen, S. Lu, K. Li, R. Kondrotas, Y. Zhao, W. Chen, L. Gao, C. Wang, J. Zhang, G. Niu, J. Tang, Vapor transport deposition of antimony selenide thin film solar cells with 7.6% efficiency, Nat. Commun. 9 (2018) 2179.

[29] R. Tang, Z.H. Zheng, Z.H. Su, X.J. Li, Y.D. Wei, X.H. Zhang, Y.Q. Fu, J.T. Luo, P. Fan, G.X. Liang, Highly efficient and stable planar heterojunction solar cell based on sputtered and post-selenized Sb_2Se_3 thin film, Nano Energy 64 (2019) 103929.

[30] M. Luo, M.Y. Leng, X.S. Liu, J. Chen, C. Chen, S.K. Qin, J. Tang, Thermal evaporation and characterization of superstrate CdS/Sb_2Se_3 solar cells, Appl. Phys. Lett. 104 (2014) 173904.

[31] S. Chen, Y. Fu, M. Ishaq, C.H. Li, D.L. Ren, Z.H. Su, X. Qiao, P. Fan, G.X. Liang, J. Tang, Carrier recombination suppression and transport enhancement enable high-performance self-powered broadband Sb_2Se_3 photodetectors, Infomat 5 (2023) 1-17.

[32] Y.D. Luo, G.J. Chen, S. Chen, N. Ahmad, M. Azam, Z.H. Zheng, Z.H. Su, M. Cathelinaud, H.L. Ma, Z.G. Chen, P. Fan, X.H. Zhang, G.X. Liang, Carrier transport enhancement mechanism in highly efficient antimony selenide thin-film solar cells, Adv. Funct. Mater. 33 (2023) 2213941.

[33] G.X. Liang, M.D. Chen, M. Ishaq, X.R. Li, R. Tang, Z.H. Zheng, Z.H. Su, P. Fan, X.H. Zhang, S. Chen, Crystal growth promotion and defects healing enable minimum open-circuit voltage deficit in antimony selenide solar cells, Adv. Sci. 9 (2022) 2105142.

[34] X.X. Wen, C. Chen, S.C. Lu, K.H. Li, R. Kondrotas, Y. Zhao, W.H. Chen, L. Gao, C. Wang, J. Zhang, G.D. Niu, J. Tang, Vapor transport deposition of antimony selenide thin film solar cells with 7.6% efficiency, Nat. Commun. 9 (2018) 2179

[35] S.C. Liu, C.M. Dai, Y.M. Min, Y. Hou, A.H. Proppe, Y. Zhou, C. Chen, S.Y. Chen, S.Y. Chen, J. Tang, D.J. Xue, E.H. Sargent, J.S. Hu, An antibonding valence band maximum enables defect-tolerant and stable GaSe photovoltaics Nat. Commun. 12 (2021) 670.

[36] X.S. Liu, X. Xiao, Y. Yang, D.J. Xue, D.B. Li, C. Chen, S.C. Lu, L. Gao, Y.S. He, M.C. Beard, G. Wang, S.Y. Chen, J. Tang, Enhanced Sb_2Se_3 solar cell performance through theory-guided defect control, Prog. Photovoltaics Res. Appl. 25 (2017) 861–870.

[37] M.L. Huang, P. Xu, D. Han, J. Tang, S.Y. Chen, Complicated and unconventional defect properties of the quasi-one-dimensional photovoltaic semiconductor Sb_2Se_3, ACS Appl. Mater. Interfaces 11 (2019) 15564–15572.

Table 1. Photovoltaic parameters of 2H, 3H, 4H, and 5H devices.

Devices	V_{OC} (V)	J_{SC} (mA/cm^2)	FF (%)	PCE (%)	R_s (kΩ)	R_{sh} (kΩ)
2H	0.540	10.99	59.59	3.52	0.078	1.723
3H	0.568	11.22	63.04	3.80	0.075	1.824
4H	0.647	17.23	51.93	5.51	0.088	1.564
5H	0.591	16.87	48.27	4.72	0.089	1.524

Table 2. EDS results for $Sb_2(S,Se)_3$ thin films with different reaction times.

Sample	Sb (at. %)	S (at. %)	Se (at. %)
2H	40.3	22.67	37.03
3H	39.01	19.76	41.23
4H	38.84	16.20	44.96
5H	40.24	12.66	47.10

Table 3. The data obtained from CV, DLCP, and TSPV measurement.

Devices	$N_{C\text{-}V}$ (cm^{-3})	N_{DLCP} (cm^{-3})	Interface defect density(cm^{-3})	V_{bi} (mV)	W_d (nm)	τ (μs)
2H	5.95×10^{15}	4.47×10^{15}	1.48×10^{15}	645	207.7	4.03
4H	2.76×10^{15}	2.02×10^{15}	7.4×10^{14}	764	276.2	7.15
5H	3.13×10^{15}	2.25×10^{15}	8.8×10^{14}	686	211.6	5.63

Table 4. Defects parameters of $Sb_2(S, Se)_3$ photovoltaic devices.

Devices	Defects	E_T (eV)	Type	σ (cm^2)	N_T (cm^{-3})	$N_T \times \sigma$ (cm^{-1})
2H	H1	E_V+0.160	V_{Sb}	9.51×10^{-16}	5.10×10^{11}	4.85×10^{-4}
4H	H1	E_V+0.386	V_{Sb}	1.09×10^{-18}	4.47×10^{11}	4.87×10^{-7}
5H	H1	E_V+0.180	V_{Sb}	2.03×10^{-17}	4.97×10^{11}	1.01×10^{-5}

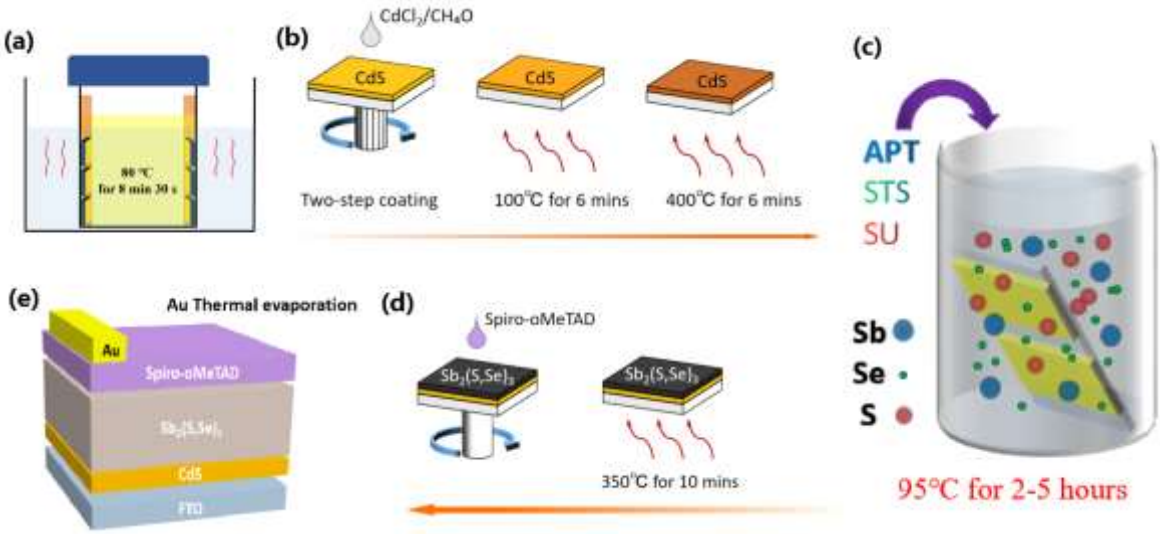

Figure 1. (a) Deposition of CdS buffer layer, (b) Spin-coating of $CdCl_2$/methanol solution, (c) Preparation of $Sb_2(S, Se)_3$, (d) Spin-coating of Spiro-oMeTAD, and (e) Deposition of $Sb_2(S, Se)_3$ devices.

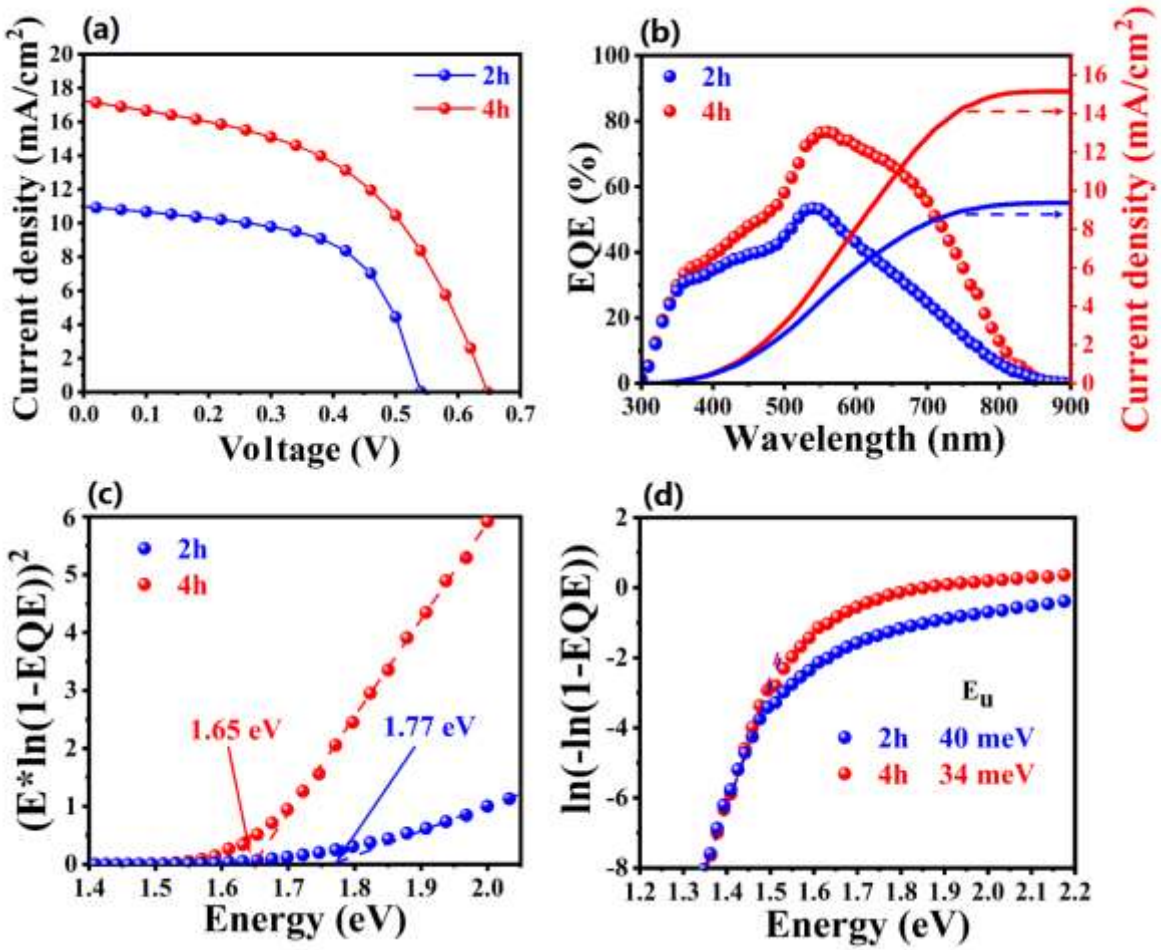

Figure 2. (a) *J-V* of 2H and 4H devices. (b) *EQE* and integrated J_{SC} of 2H and 4H devices. (c) bandgap obtained from the *EQE* of 2H and 4H devices, and (d) urbach energy calculated from the EQE of 2H and 4H devices.

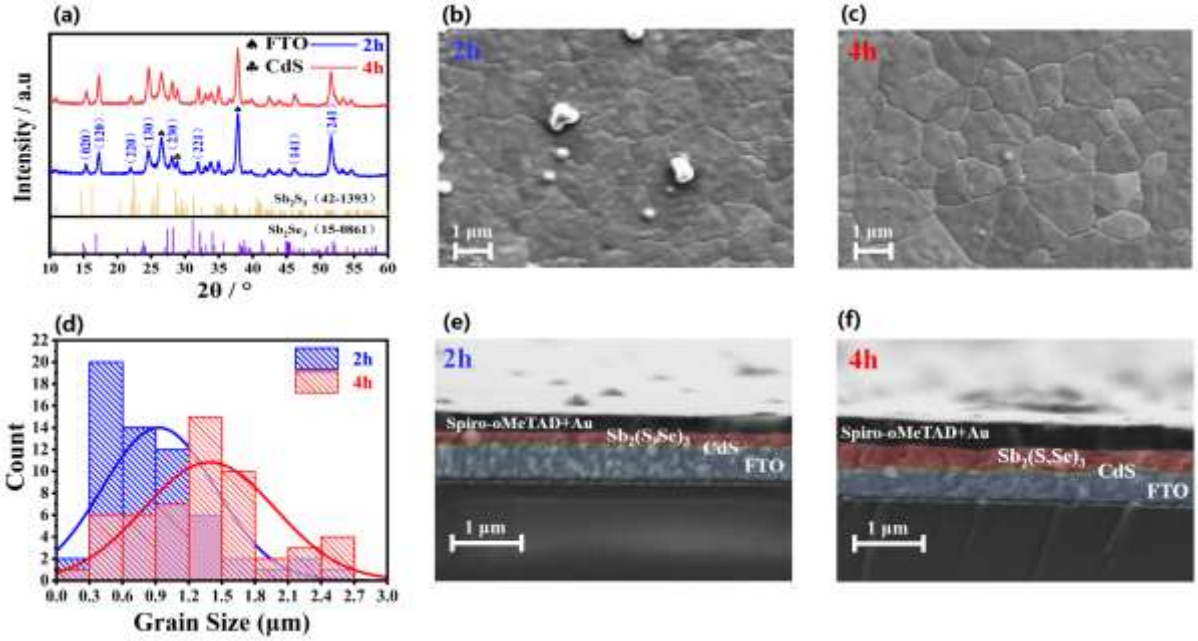

Figure 3. (a) XRD patterns of 2H and 4H solar cells, (b) Surface morphologies of $Sb_2(S,Se)_3$ absorber with reaction times of 2h, (c) Surface morphologies of $Sb_2(S,Se)_3$ with reaction times of 4h, (d) The statistical distribution of the $Sb_2(S,Se)_3$ grain size with reaction times of 2h and 4h. (e) Cross morphologies of (e) 2H and (f) 4H solar cells.

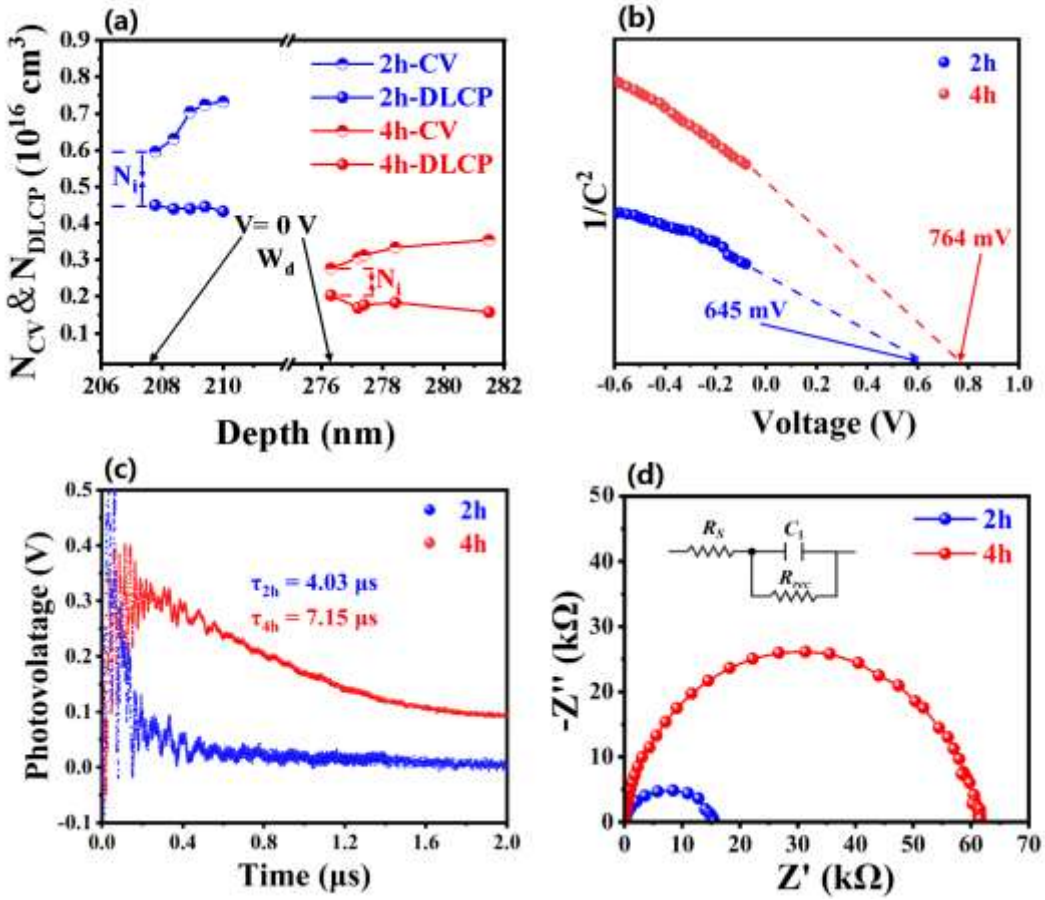

Figure 4. (a) *C-V* and *DLCP* of 2H and 4H solar cells. (b) $1/C^2$-V curves of the 2H and 4H solar cells. (c) TSPV plots of 2H and 4H solar cells. (d) Nyquist plots of 2H and 4H solar cells.

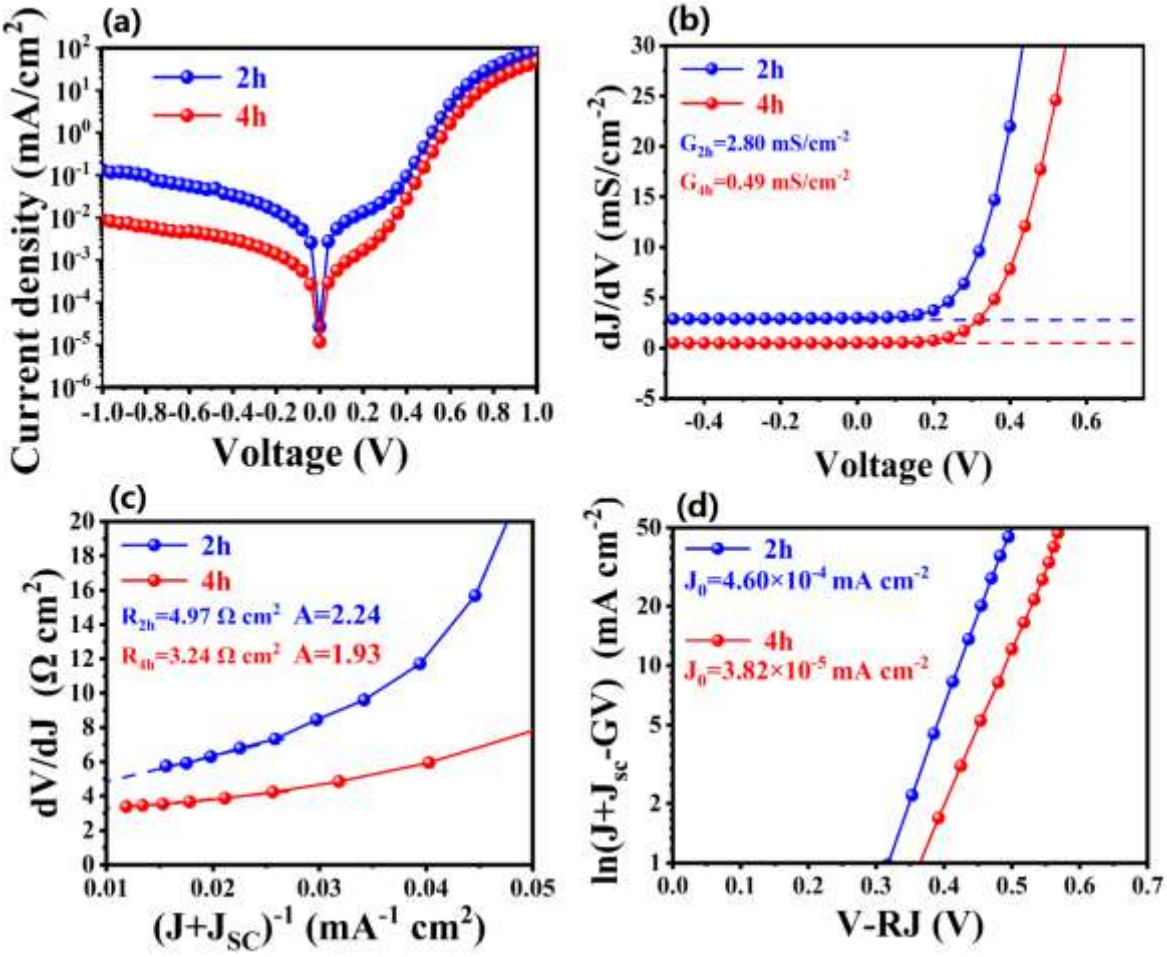

Figure 5. (a) Dark *J-V*, (b) shunt conductance *G*, (c) series resistance R_s and ideality factor *A*, and (d) reverse saturation current density J_0 of 2H and 4H solar cells.

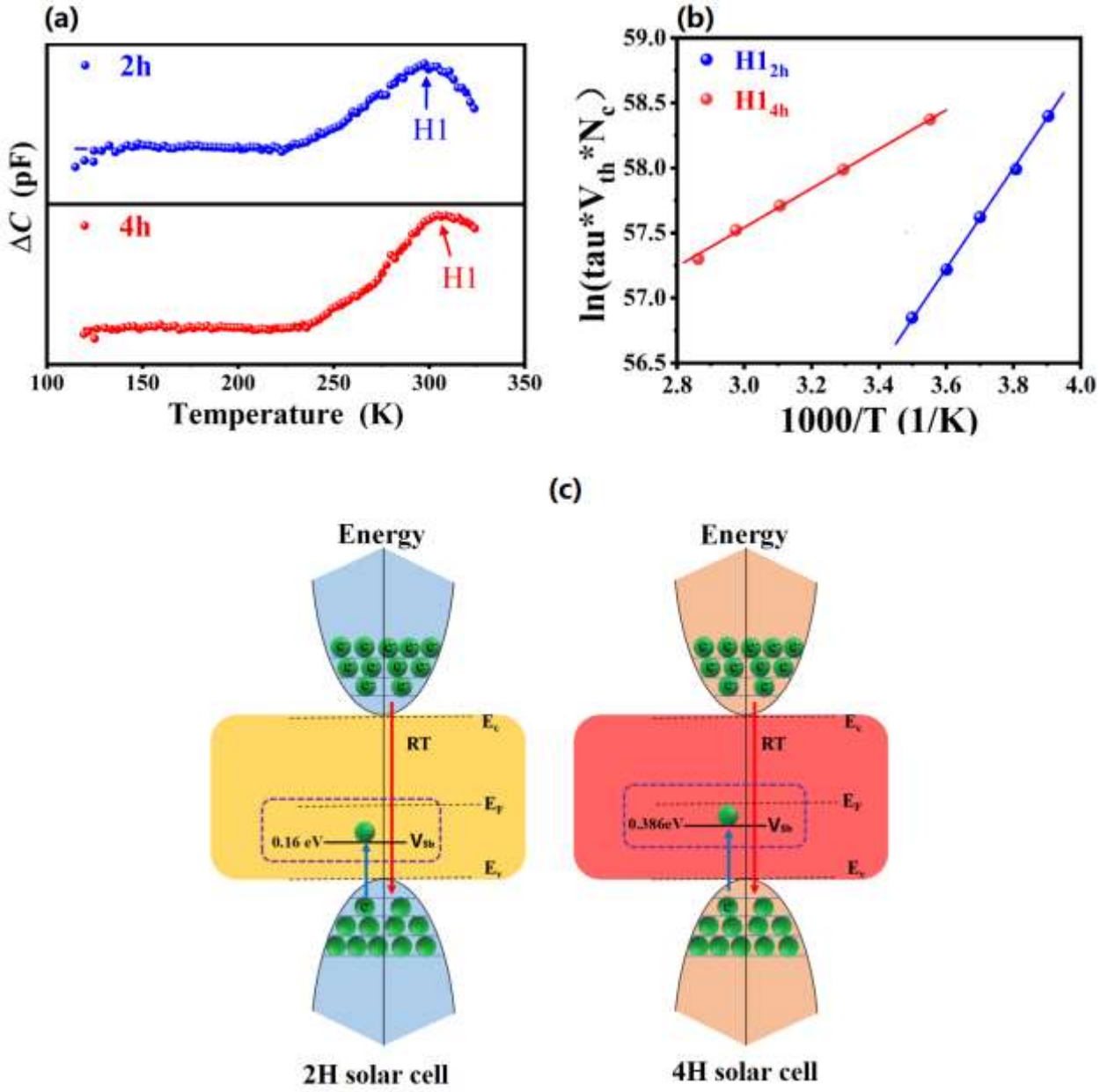

Figure 6. (a) DLTS signals from 2H and 4H solar cells. (b) The Arrhenius plots were calculated from DLTS of 2H and 4H solar cells. (c) Conduction band (E_C) and valence band (E_V), and defect energy levels of 2H and 4H solar cells.

Graphical Abstract

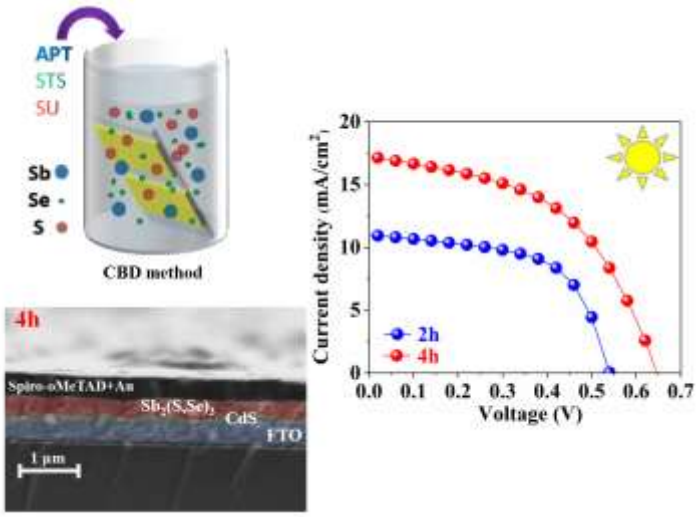

Declaration of interests

☒ The authors declare that they have no known competing financial interests or personal relationships that could have appeared to influence the work reported in this paper.

☐The authors declare the following financial interests/personal relationships which may be considered as potential competing interests: